Topology Optimization simulation for Double wishbone Suspension A-Arm and Component Additive Manufacturing

El Mehdi Adib Alaoui

December 2025

1 Abstract

The increasing adoption of additive manufacturing (AM) in the automotive sector enables lightweight, functionally integrated components and shorter development cycles compared to traditional manufacturing [1]. In suspension systems, AM has been used to redesign wheel and suspension structures with integrated conductions and improved load paths, revealing outstanding potential for weight reduction and part consolidation [2]. Direct metal AM of automotive parts further supports the production of structurally efficient, topology optimized geometries tailored to specific load cases while matching performance and reliability requirements [1, 3].

AM encompasses a family of layer-wise processes such as powder bed fusion, material extrusion, vat photopolymerization and binder jetting, each with characteristic resolutions, build rates and thermal histories that influence part properties [4]. These processes can produce parts from polymers, metals, ceramics and composites, providing designers with a spectrum of materials whose stiffness, strength and durability depend strongly on process parameters and scan strategies [4, 5]. In manufacturing and construction contexts, the tight integration of CAD, slicing and toolpath generation within a digital workflow shifts many design constraints from traditional tooling toward process-specific limitations such as support generation, build orientation and layer induced anisotropy [6]. As a result, structural components intended for AM must be evaluated with respect to these process dependent constraints, motivating simulation driven design and topology optimization (TO) frameworks that explicitly incorporate AM capabilities and limitations [5, 6].

(AM) overview studies report a transition from rapid prototyping to functional production components across multiple manufacturing industries, driven by opportunities for part consolidation, design customization and reduced tooling requirements [5]. In the construction sector, AM-enabled digital workflows and layer-wise deposition strategies are used to realise structurally efficient forms, internal channels and graded sections that align with architectural and structural performance targets [6]. Parallel developments in the aerospace and automobile sectors show that similar capabilities are exploited to produce lightweight, high-performance components and to shorten development cycles, providing a broader technological context for applying AM-informed topology optimisation to automotive suspension structures in this work [5, 7].

2 Introduction

Additive manufacturing (AM), or 3D printing, has become an important manufacturing route in the aerospace and automobile sectors, where components are built directly from CAD data by depositing material layer by layer [7]. In metal AM, the combination of high design freedom, geometric complexity, lightweighting potential and part consolidation enables highly integrated suspension and chassis structures that are difficult to obtain with conventional subtractive methods [8]. These capabilities make AM particularly attractive for re-engineering load-bearing systems such as automotive suspension arms, where mass reduction and functional integration must be achieved while maintaining structural stiffness and durability [7]. At the same time, multi-scale and multi-physics simulations of metal AM processes have shown that numerical models can predict thermal histories, residual stresses and defect formation across different length scales, offering a robust tool for process understanding and quality assurance [9]. Building on these developments, the present work investigates topology-optimized automotive suspension components tailored for metal AM, coupling structural optimization of an A-arm with process-aware analysis to assess both manufacturability and in-service performance.

Modeling and simulation play a central role in exploiting metal additive manufacturing for structurally efficient components, with reviews classifying approaches into thermal, thermo-mechanical, microstructural and geometric models that capture different aspects of the layer-wise process [10]. Multi-scale and multi-physics frameworks further couple melt-pool scale heat transfer and fluid flow to part-scale stress and distortion predictions, enabling more accurate estimation of residual stresses, dimensional accuracy and defect formation

in complex geometries [9]. At larger scales, research on multi-robot additive manufacturing uses path-planning optimisation, deposition-sequence scheduling and interference avoidance strategies to coordinate multiple print heads over a shared build space, demonstrating how algorithmic control and simulation can significantly improve build efficiency for large structures [11]. Motivated by these simulation-centric practices, the present work imports an existing suspension A-arm in STEP format and applies a sequential ANSYS-based pipeline—baseline structural finite element analysis, density-based topology optimisation, SpaceClaim geometry clean-up and autofix, and final validation simulations—to obtain an AM-suitable design that satisfies stiffness and strength requirements.

From an industrial perspective, recent reviews on additive manufacturing in the automobile sector describe how major manufacturers are progressively integrating AM across prototyping, tooling and low-volume component production, while also highlighting market drivers such as electrification, customization and sustainability [12]. Development-oriented surveys further emphasize that the adoption of AM technology in the automotive field depends on expanding printable materials, improving process stability and quality control, and reducing overall manufacturing cost to move from demonstrators toward broader deployment [13]. In parallel, advances in gradient-structured metals and alloys demonstrate that tailored microstructural architectures can deliver enhanced combinations of strength, ductility and fatigue resistance, offering promising material systems for highly loaded AM components [14]. Within this landscape, a topology-optimised suspension A-arm designed explicitly for metal AM contributes a component-level case study that connects emerging materials and industrial adoption trends with simulation-driven structural design for automotive applications [12, 13, 14].

3 Background

Additive manufacturing is increasingly embedded in digitally driven, green automotive production, where national and industrial roadmaps identify AM as a core technology for shortening development cycles, improving part quality, and enabling lightweight designs in highly competitive vehicle markets [13]. Recent mini-reviews focused on the automotive sector further summarize the range of AM processes already deployed—such as FFF, SLS, SLM, Binder Jetting and SLA—and discuss their use in functional vehicle parts, rapid prototyping and electric-vehicle components, while also emphasizing limitations in build size, production volume, material/process robustness, post-processing effort and standardization as key challenges for broader industrial adoption [15]. Beyond process adoption, recent materials research on gradient-structured metals and alloys shows that tailoring heterogeneous microstructures can simultaneously enhance strength, ductility and fatigue resistance, offering a pathway to durable yet lightweight suspension links and chassis components [14]. At the manufacturing-system level, large-scale AM concepts based on multi-robot collaboration address build-envelope and productivity limitations of single-machine platforms, coordinating multiple deposition robots to fabricate complex structures with higher efficiency [11]. Together, these developments in automotive AM practice, advanced metallic materials and scalable manufacturing architectures motivate the present study on topology-optimized, additively manufacturable suspension A-arms that can eventually exploit gradient alloys and large-format metal AM systems [11, 13, 14, 15].

4 Objectives

The present work has the following objectives:

- To perform a linear static structural analysis in ANSYS Mechanical on an existing suspension A-arm in order to establish a baseline response in terms of von Mises stress distribution, total deformation patterns and deformation magnitudes under representative load cases.
- To carry out density-based topology optimisation of the A-arm, using the baseline structural response as input, with the goal of reducing mass while constraining stiffness and stress levels.
- To target an approximate 20% reduction in component mass in order to increase the natural frequency of the arm–wheel assembly, reduce inertial and self-weight loads, and decrease additive manufacturing build time and material consumption, as discussed in the theoretical framework.
- To reconstruct and clean the optimised geometry and to validate the redesigned A-arm through repeated static structural and fatigue analyses, verifying that the topology-optimised component theoretically maintains comparable performance to the baseline design in terms of von Mises stresses, total deformation and fatigue metrics (life and equivalent alternating stress).
- To assess the suitability of candidate AM materials and processes for manufacturing the optimised A-arm by constructing a material performance index and applying a decision matrix that combines mechanical properties, density and AM-specific constraints.

5 Theoretical framework

From a vibration standpoint, reducing the mass of the suspension A-arm has a direct impact on its natural (resonant) frequency. Approximating the arm–wheel assembly locally as a single degree-of-freedom system with equivalent stiffness k and mass m, the undamped natural circular frequency ω_n and frequency f_n are

$$\omega_n = \sqrt{\frac{k}{m}}, \qquad f_n = \frac{1}{2\pi}\sqrt{\frac{k}{m}}. \tag{1}$$

For a given stiffness k, decreasing the mass m increases f_n. In this study, the topology optimisation is therefore formulated to achieve approximately 20% mass reduction. If the initial mass is m_0 and the optimised mass is $m_{opt} = 0.8\, m_0$, the ratio of natural frequencies is

$$\frac{f_{opt}}{f_0} = \sqrt{\frac{m_0}{m_{opt}}} = \sqrt{\frac{1}{0.8}} \approx 1.12, \tag{2}$$

which corresponds to an increase of about 12% in natural frequency for the same stiffness. A higher natural frequency shifts resonance away from typical road-excitation and operating frequencies, reducing the risk of large vibration amplitudes in the suspension links and bushings.

A second benefit of mass reduction is the decrease in inertial forces. For a given acceleration a, the inertial force associated with the A-arm mass is

$$F_{inertia} = m\, a. \tag{3}$$

With $m_{opt} = 0.8\, m_0$ and the same acceleration a, the force ratio is

$$\frac{F_{opt}}{F_0} = \frac{m_{opt}}{m_0} = 0.8, \tag{4}$$

so the inertial contribution to joint loads and internal forces is reduced by 20%. The same proportional reduction applies to the self-weight of the arm, $W = mg$, and to bending moments generated by that self-weight, which are directly proportional to W.

In a simplified unsprung-mass model, the vertical natural frequency of the unsprung assembly can be written as

$$f_u = \frac{1}{2\pi}\sqrt{\frac{k_t}{m_u}}, \tag{5}$$

where k_t is the effective tyre stiffness and m_u is the unsprung mass (wheel, brake, arm and associated hardware). Reducing the A-arm contribution to m_u leads to

$$\frac{f_{u,opt}}{f_{u,0}} = \sqrt{\frac{m_{u,0}}{m_{u,opt}}}, \tag{6}$$

so that a lower unsprung mass shifts the unsprung natural frequency upward and improves wheel contact with the road surface for the same excitation spectrum.

Finally, for metal additive manufacturing processes such as laser powder bed fusion, both build time t_{build} and powder consumption m_{powder} scale approximately with the part volume (and hence mass). Assuming constant process parameters,

$$t_{build,opt} \approx 0.8\, t_{build,0}, \qquad m_{powder,opt} \approx 0.8\, m_{powder,0}, \tag{7}$$

for a 20% mass reduction. This directly translates into shorter build times, lower material usage and reduced manufacturing cost. Taken together, the increased natural frequency, reduced inertial and self-weight loads, improved unsprung-mass characteristics and lower AM process effort provide a theoretical justification for targeting a 20% reduction in component mass while maintaining or improving the structural performance of the suspension system.

6 Methodology

The proposed methodology follows a simulation-driven workflow that starts from a CAD-based suspension component and progressively refines it into an additively manufacturable, structurally verified design. The baseline double-wishbone A-arm is first imported in STEP format and checked in SolidWorks for dimensional consistency and critical geometric features, after which it is transferred to ANSYS Mechanical for material assignment, mesh-convergence studies and linear static finite element analysis to obtain von Mises stress and deformation fields under representative suspension load cases. Similar FE-based verification of load-bearing AM

components is routinely employed before fabrication in recent automotive suspension and bracket case studies [2, 3]. Based on these results, a density-based topology optimisation is performed in ANSYS to minimise compliance subject to volume and stress constraints, consistent with literature where topology optimisation is coupled with AM to reduce mass while maintaining structural performance [2]. The optimised density field is then exported to SpaceClaim for facet and overlap clean-up, autofix and shrink-wrap operations, followed by reconversion to a watertight solid that respects minimum feature sizes and other AM-related geometric constraints. This interpreted geometry is re-imported into ANSYS Mechanical for validation simulations, where the redesigned A-arm is evaluated through stress, displacement and a material performance index combining mass and stiffness, an approach aligned with multi-scale and multi-physics modelling frameworks that link geometry, loading and predicted mechanical response in metal AM structures [9, 10]. If target performance is satisfied, the validated model proceeds to slicer configuration for subsequent AM process planning.

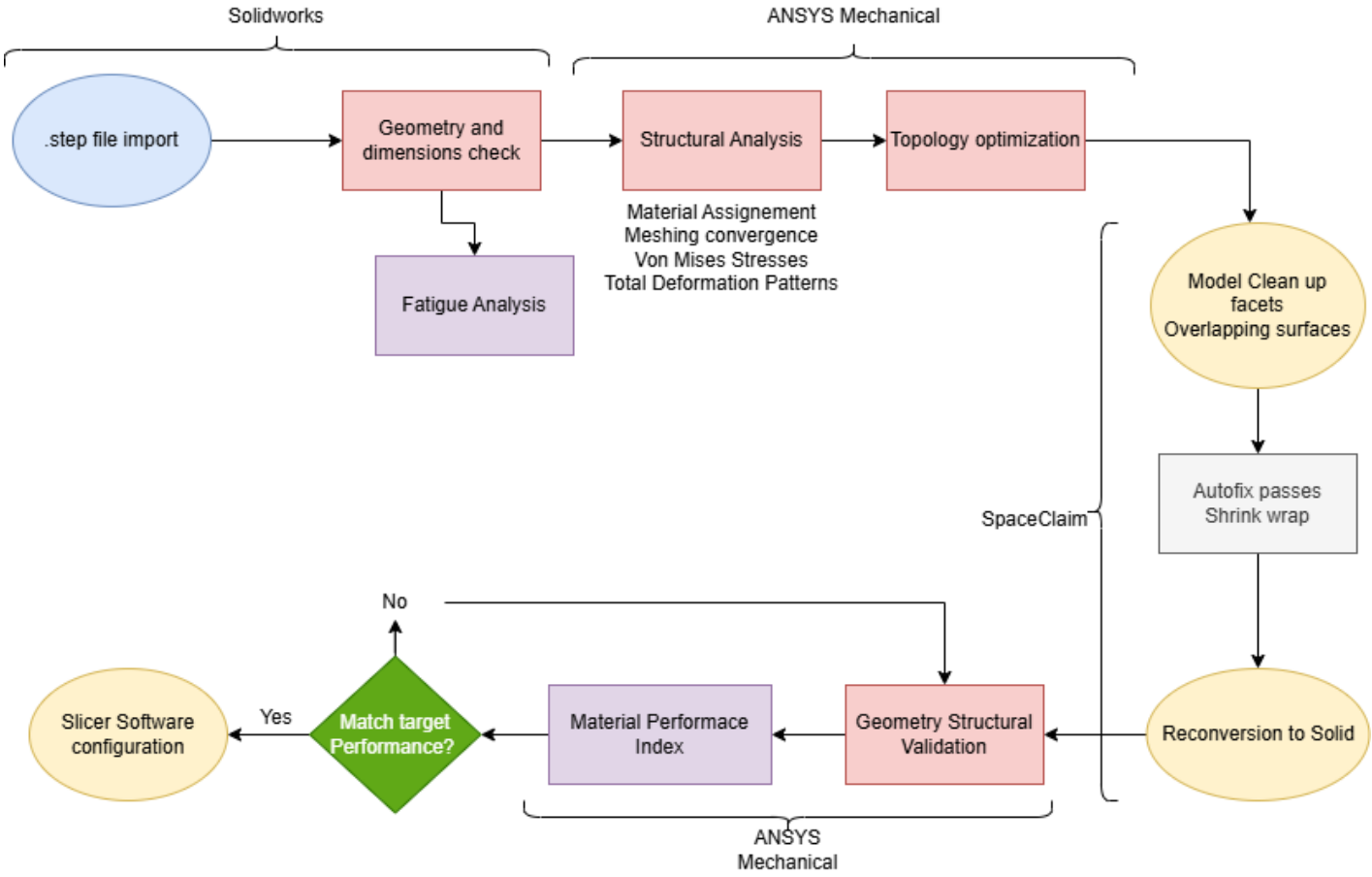

Figure 1: Simulation and design workflow for a topology-optimised, additively manufacturable suspension A-arm.

The ANSYS Workbench project is organised into three linked systems: an initial static structural analysis, a topology optimisation system that reuses the same engineering data and geometry, and a final static structural system for validation of the optimised design.

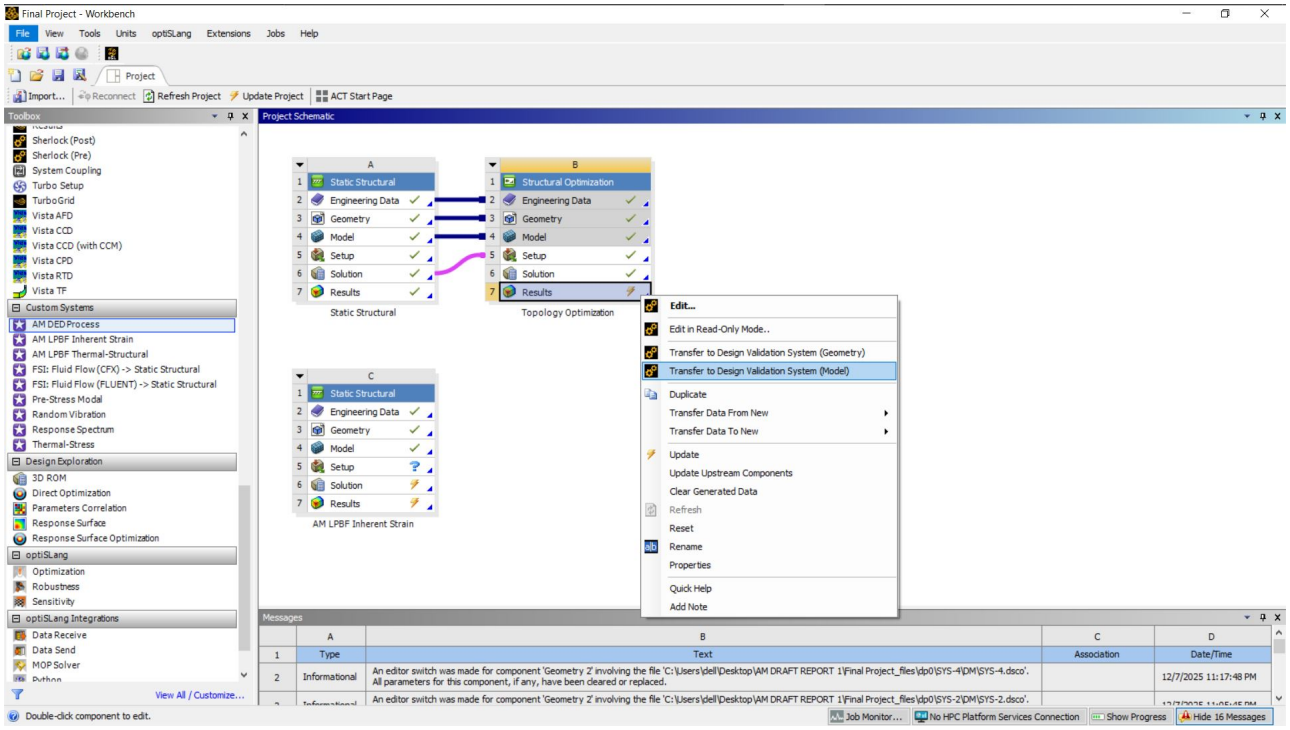

Figure 2: ANSYS Mechanical environment used for structural validation of the optimised geometry.

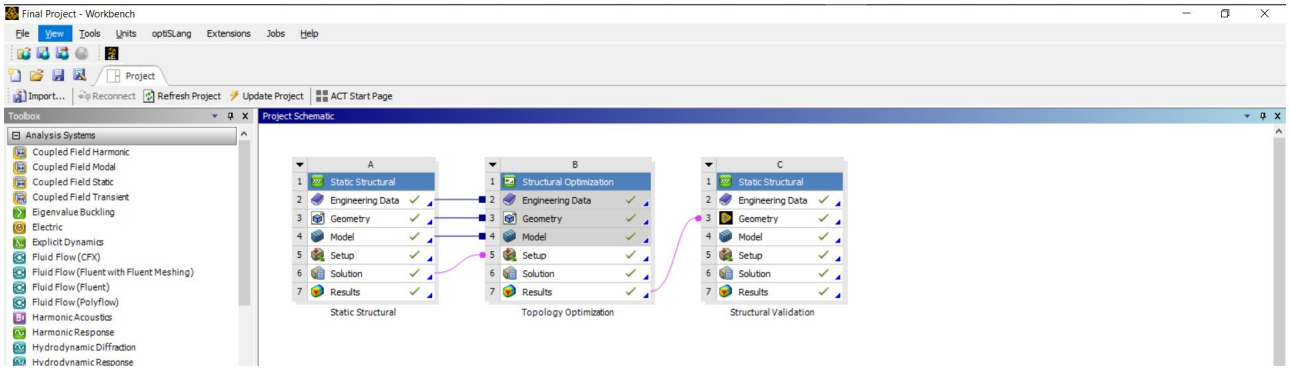

Figure 3: Simulation and design workflow for the topology-optimised suspension A-arm.

7 Double Wishbone Suspension A-Arm component dimensions

The baseline geometry of the simulated component, referred to as the *Plan*, is shown in Figure 4. The part is a front suspension A-arm with a Y-shaped layout, where the two chassis-side bushings are spaced approximately 251.54mm apart and connected to the wheel-side bushing by curved arms of length about 158.38mm. The overall span from the rear chassis joint to the wheel-side joint is about 303.54mm, while the arm thickness in the vertical direction is on the order of 50mm, giving a relatively slender bending member. Large fillet radii (e.g. $R110$ and $R27.77$) smooth the load path between the arms and the central pocket region, reducing local stress concentrations, and the cylindrical interfaces for the bushings (diameters 36mm, 30mm and 48mm) define the mechanical joints through which suspension loads are transmitted. These dimensions collectively establish the stiffness, lever arm and packaging constraints of the A-arm and form the reference geometry for the subsequent finite element analysis and topology optimisation.

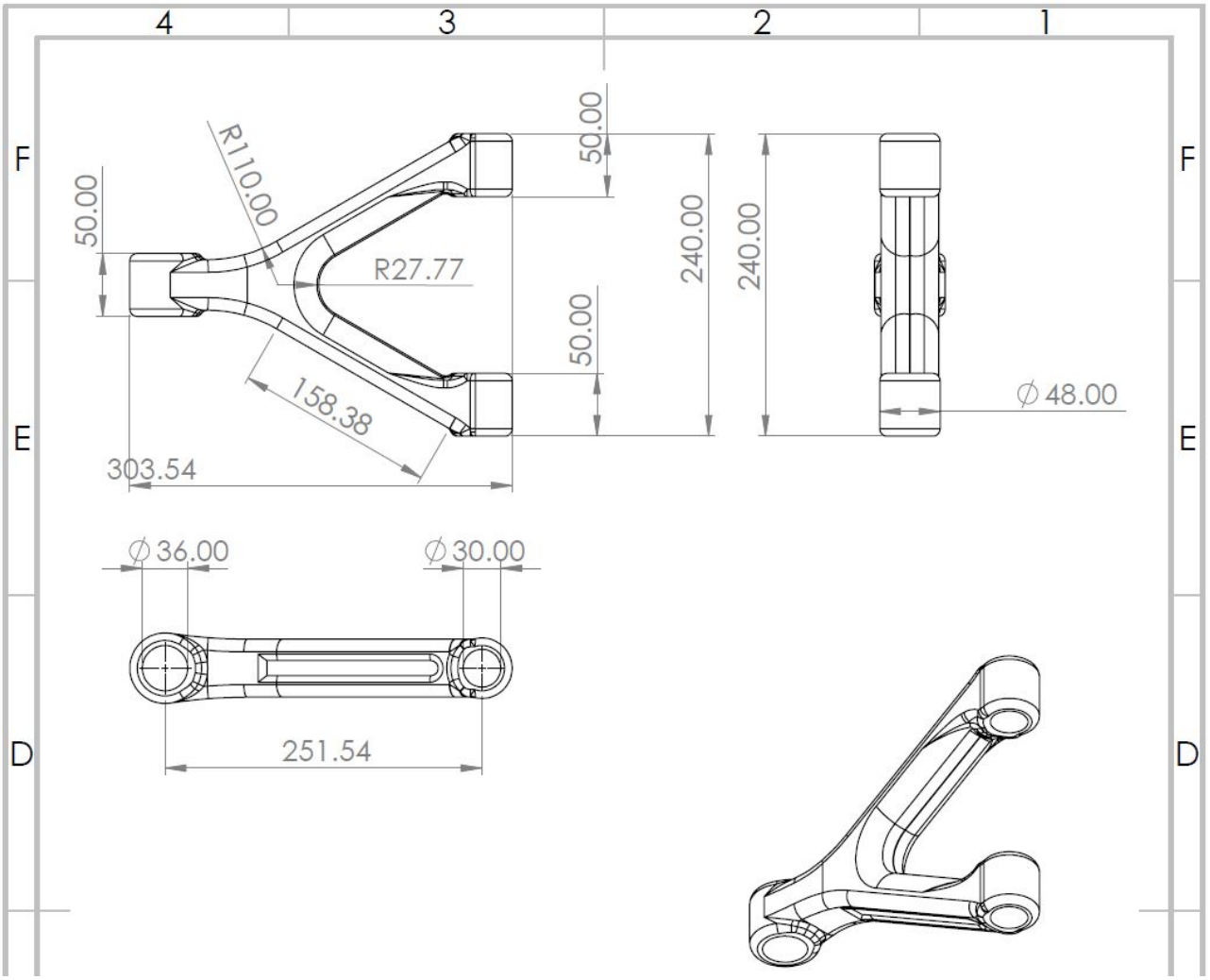

Figure 4: Plan and orthographic views of the baseline suspension A-arm (*Plan*) with key dimensions.

8 Simulation Setup

In the baseline static structural setup, the inner bushing of the A-arm is constrained with a *Fixed Support*, so all translational and rotational degrees of freedom are suppressed at the chassis-side joint. On the opposite bushing, a surface-based pressure load of 5e6Pa is applied to the inner cylindrical face in the global loading direction, converting to a distributed resultant force that represents the combined wheel-side reaction transmitted through the joint. Because the load is imposed as a uniform pressure rather than a point force, it is spread over the contact surface and avoids artificial stress concentrations at individual nodes. Together, these boundary conditions idealise the A-arm as a cantilevered link fixed at the chassis and loaded through the wheel joint,

providing a representative suspension loading scenario for evaluating von Mises stress and total deformation (Figure 5).

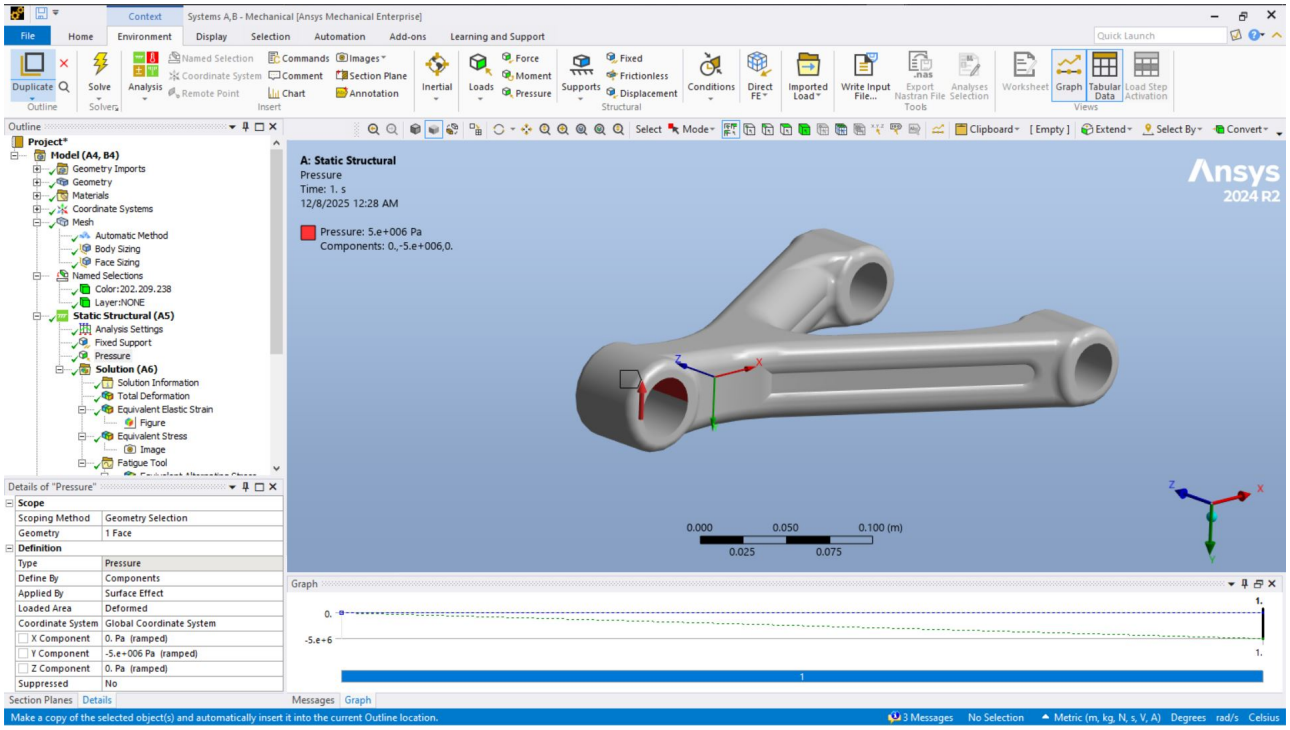

Figure 5: Applied boundary conditions for the baseline static structural analysis of the A-arm.

9 Structural Analysis Results

Result1 – Total deformation

The total deformation plot in Figure 6 shows the global bending response of the baseline A-arm under the applied load case. The maximum displacement is approximately 1.2mm at the loaded outer bushing, while the inner bushing at the chassis side remains essentially fixed. This smooth deflection shape confirms the expected cantilever-like behaviour of the component and provides a reference for later comparison with the topology-optimised geometry.

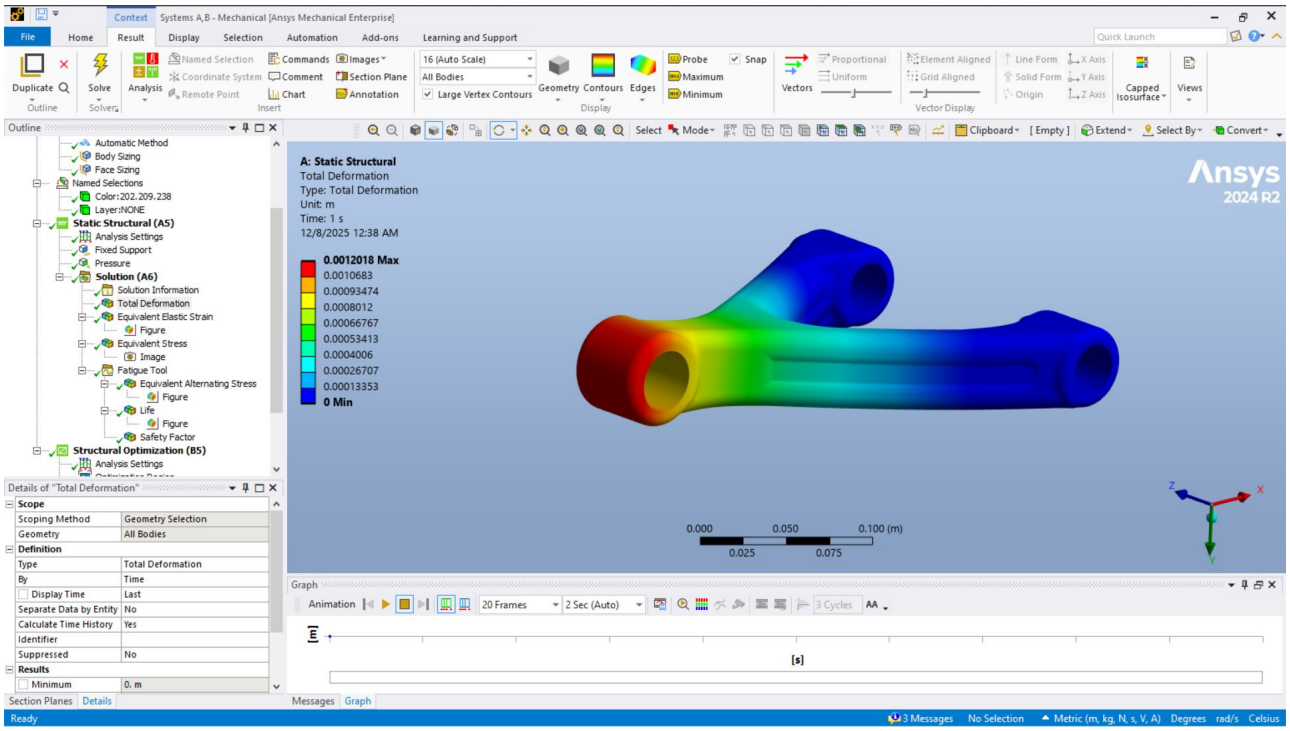

Figure 6: Result1 – total deformation of the baseline A-arm under the static load case.

Result2 – Equivalent elastic strain

Figure 7 presents the equivalent elastic strain distribution for the same loading. Elevated strain levels are concentrated around the fillet regions near the bushings and at the junction where the two arms meet, while the mid-span of the arms experiences significantly lower strain. The peak equivalent elastic strain is on the order of 10^{-3}, indicating purely elastic behaviour for typical metallic suspension materials and highlighting the geometric transitions that govern local stiffness.

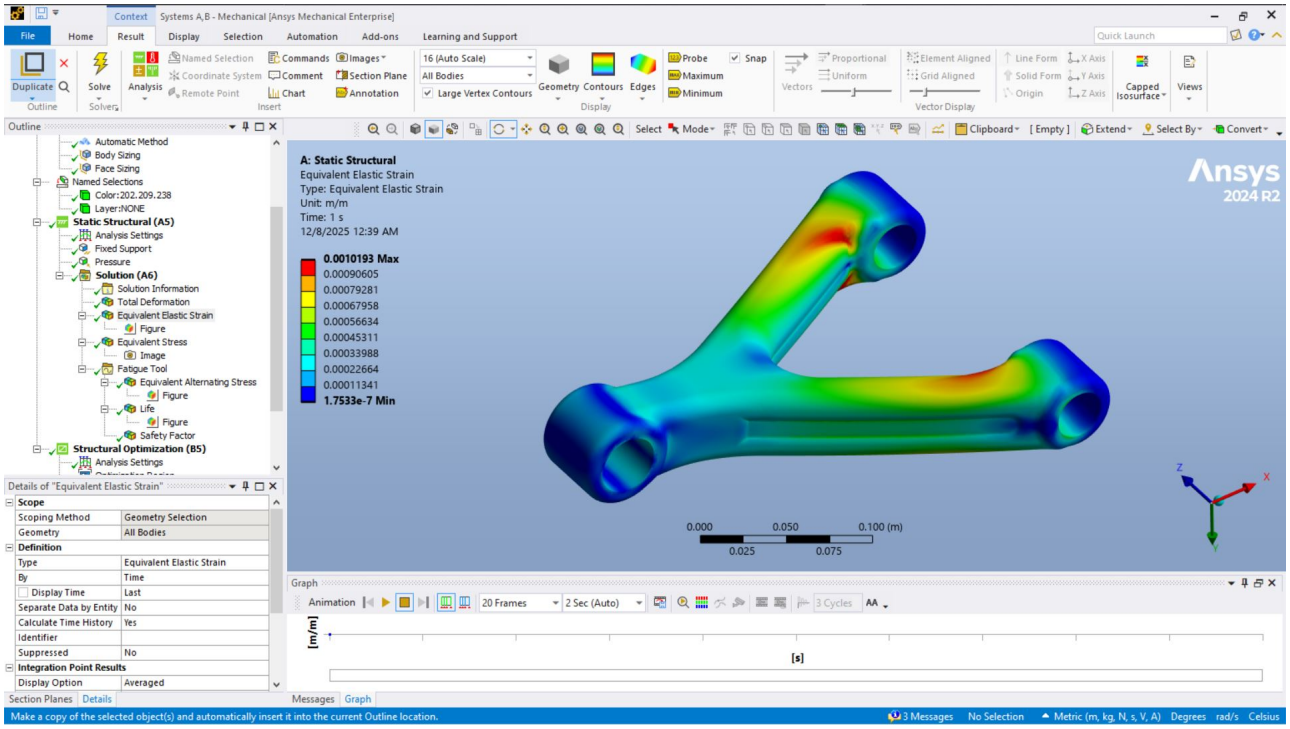

Figure 7: Result2 – equivalent elastic strain distribution in the baseline A-arm.

Result3 – Equivalent (von Mises) stress

The equivalent (von Mises) stress field in Figure 8 follows a similar pattern, with maximum stresses of about 2.0e8Pa located in the same fillet and junction regions identified in the strain plot. Large areas of the arms carry considerably lower stresses, suggesting potential for material removal in those zones. These stress hot spots therefore define the critical regions for static strength and motivate the subsequent topology optimisation to redistribute material while controlling peak von Mises stress.

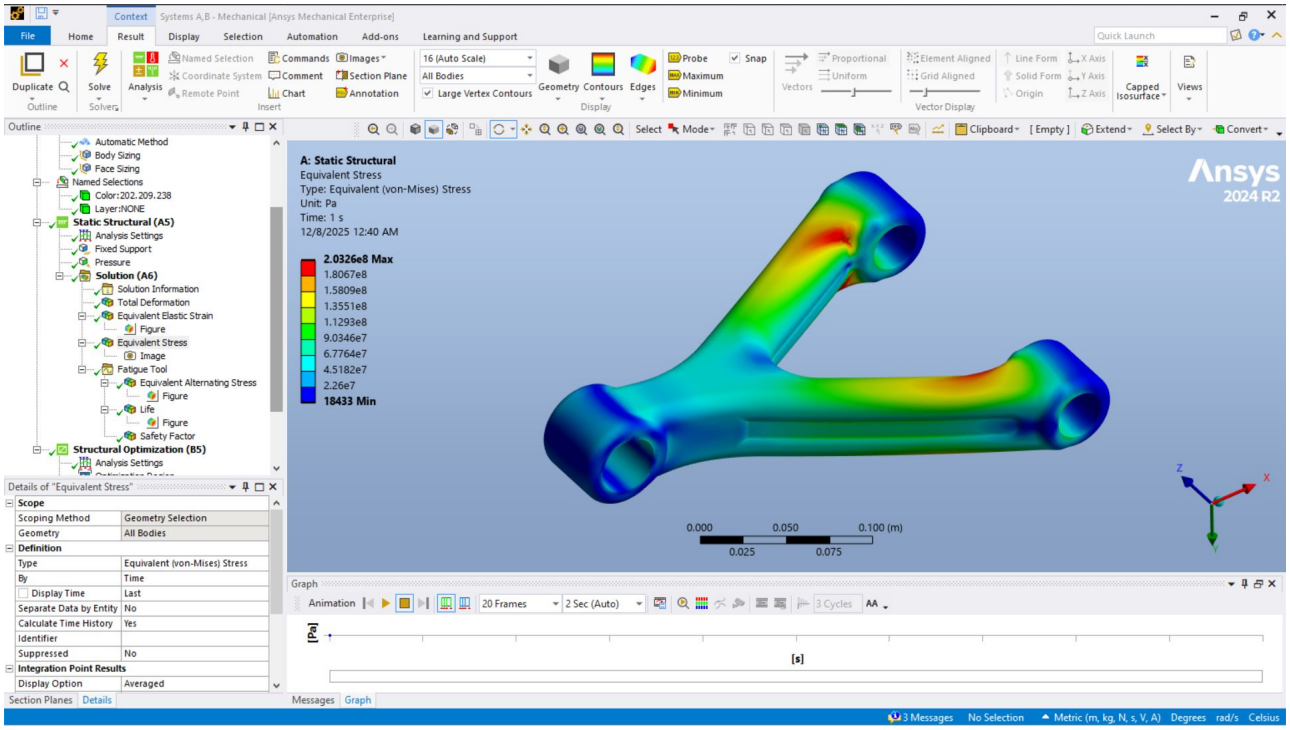

Figure 8: Result3 – equivalent von Mises stress distribution in the baseline A-arm.

10 Fatigue Analysis Results

The fatigue life results in Figure 9 (Life1) indicate a minimum life of about 2.4e4 cycles concentrated at the inner fillet near the loaded bushing, while most of the arm remains well above 1e5 cycles. The equivalent alternating stress distribution in Figure 10 (Life2) shows a matching hotspot in the same fillet region, confirming that this transition governs the fatigue performance of the baseline A-arm.

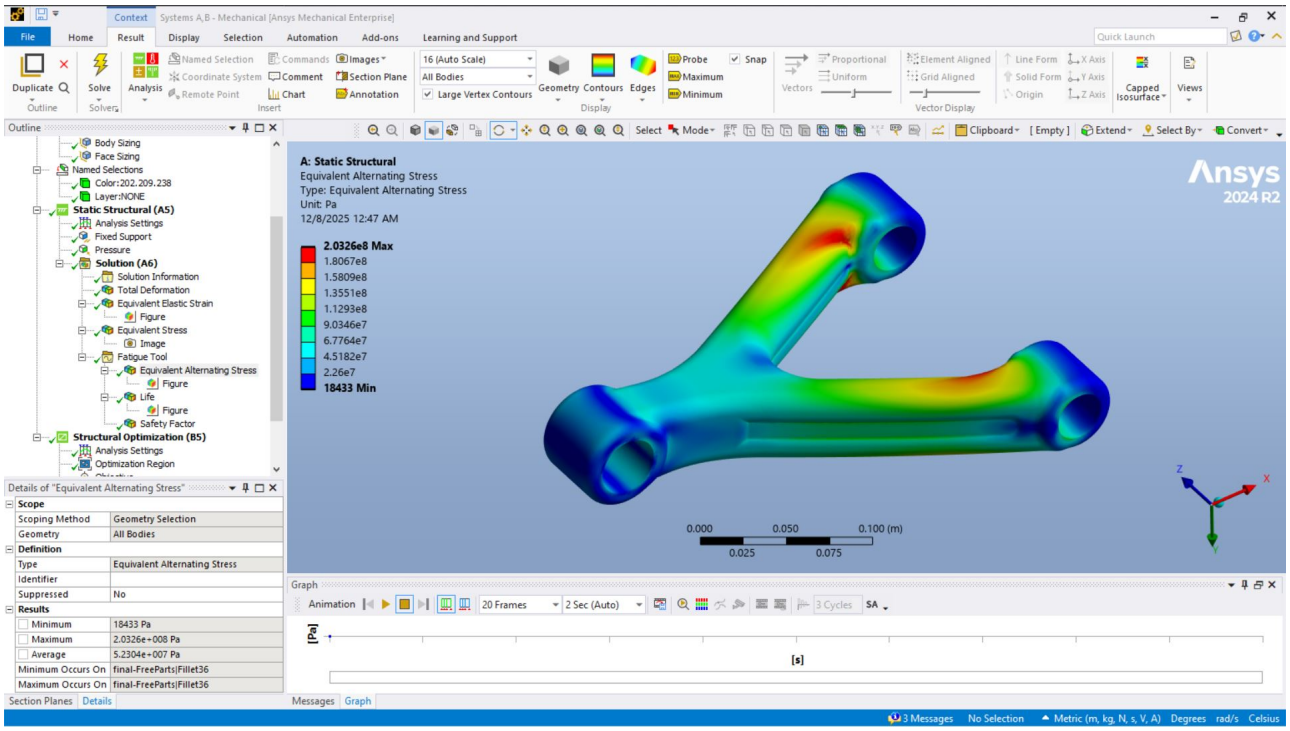

Figure 9: Life1 – predicted fatigue life distribution for the baseline A-arm.

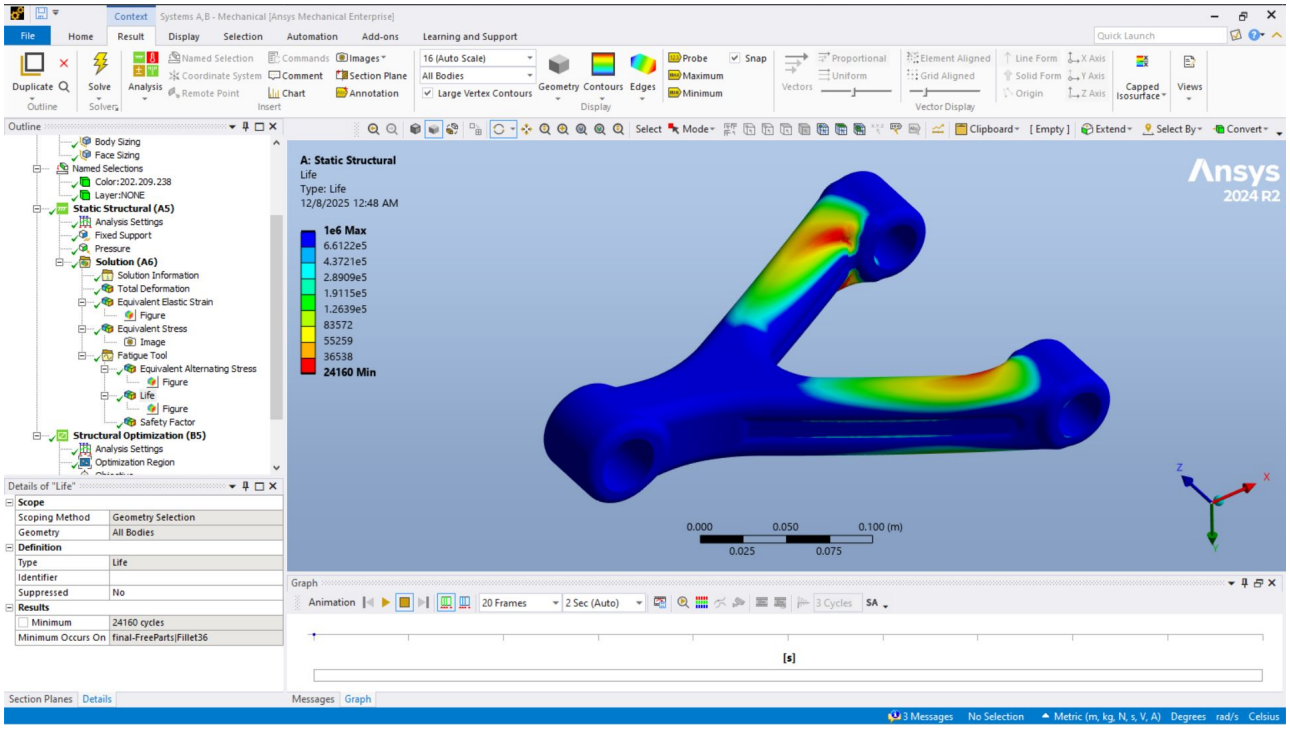

Figure 10: Life2 – equivalent alternating stress distribution in the baseline A-arm.

11 Topology Optimization Setup

11.1 Region – Optimisation region definition

For the topology optimisation step, the optimisation region is defined as the solid volume of the A-arm excluding the functional interfaces, as illustrated in Figure 11. The blue area represents the design region in which the

density-based algorithm is allowed to remove or retain material, while the red exclusion regions correspond to the bushing contact surfaces and end faces that must remain unchanged to preserve mounting geometry, load application areas and boundary conditions. By freezing these twelve interface faces, the optimisation can redistribute material only within the structural links between the joints, ensuring that the resulting topology-optimised geometry remains compatible with the original suspension assembly and can be directly compared with the baseline design.

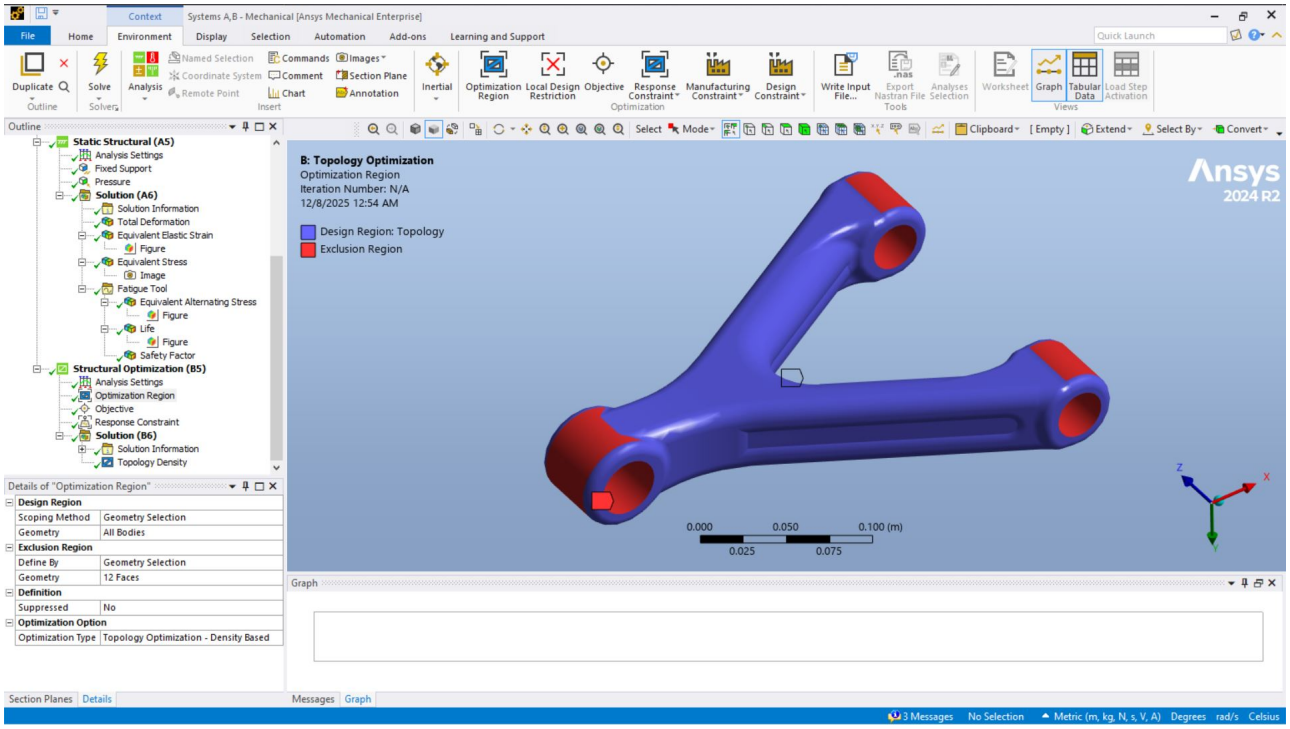

Figure 11: Region – design (blue) and exclusion (red) regions used in the topology optimisation setup.

Retain – Mass response constraint

In the topology optimisation setup, the response constraint is defined on the *Mass* of the optimisation region with a *Percent to Retain* of 80%, as shown in Figure 12. This setting limits the algorithm to remove at most around 20% of the baseline mass while minimising compliance, ensuring that the optimised A-arm remains sufficiently bulky to satisfy the static strength and fatigue requirements identified in the baseline analysis. Similar mass-constrained topology optimisation strategies are reported for additively manufactured suspension and bracket components, where weight reduction must be balanced against stiffness and stress limits [2, 3].

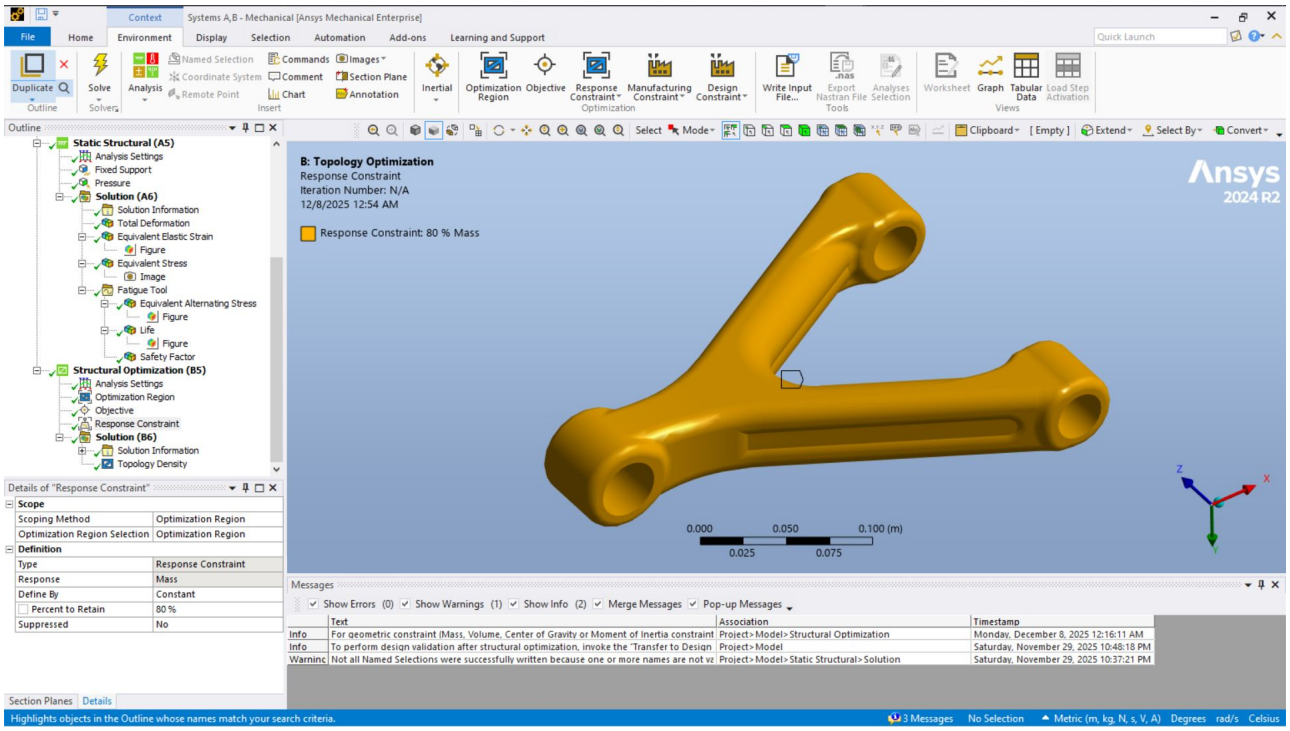

Figure 12: Retain – topology optimisation response constraint with 80% mass retained in the design region.

Settings – Topology optimisation parameters

The topology optimisation analysis settings, shown in Figure 13, use a maximum of 500 iterations with a minimum normalised density of 10^{-3} and a convergence accuracy of 5e-2, providing enough iterations for the density field to stabilise while avoiding excessive computational cost. A penalty factor of 3 is adopted for the SIMP scheme to promote a clear black–white material distribution, which is standard practice for stiffness-driven topology optimisation. Manufacturing constraints are set to *Include Exclusions*, while minimum member size and AM overhang constraints are applied only to the design region, and a program-controlled filter is used to suppress checkerboarding and mesh-dependent artefacts.

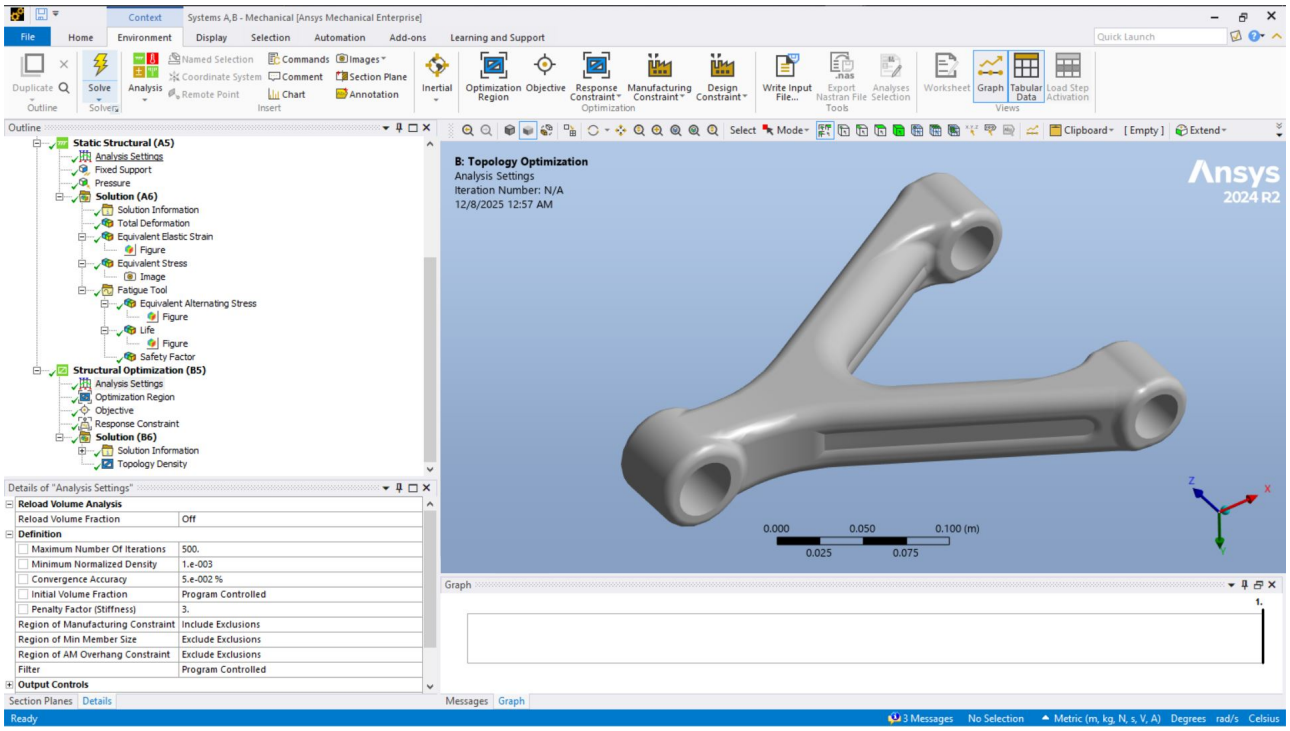

Figure 13: Settings – topology optimisation analysis parameters in ANSYS.

12 SpaceClaim geometry clean-up and export

Shrinkwrap

After importing the topology-optimised density field into SpaceClaim, a *Shrinkwrap* operation is applied to generate a watertight faceted body around the iso-surface of the material distribution, as shown in Figure 15. This step removes internal voids and highly irregular cells while preserving the overall topology, producing a single, closed triangular mesh that is suitable for further geometric repair and conversion.

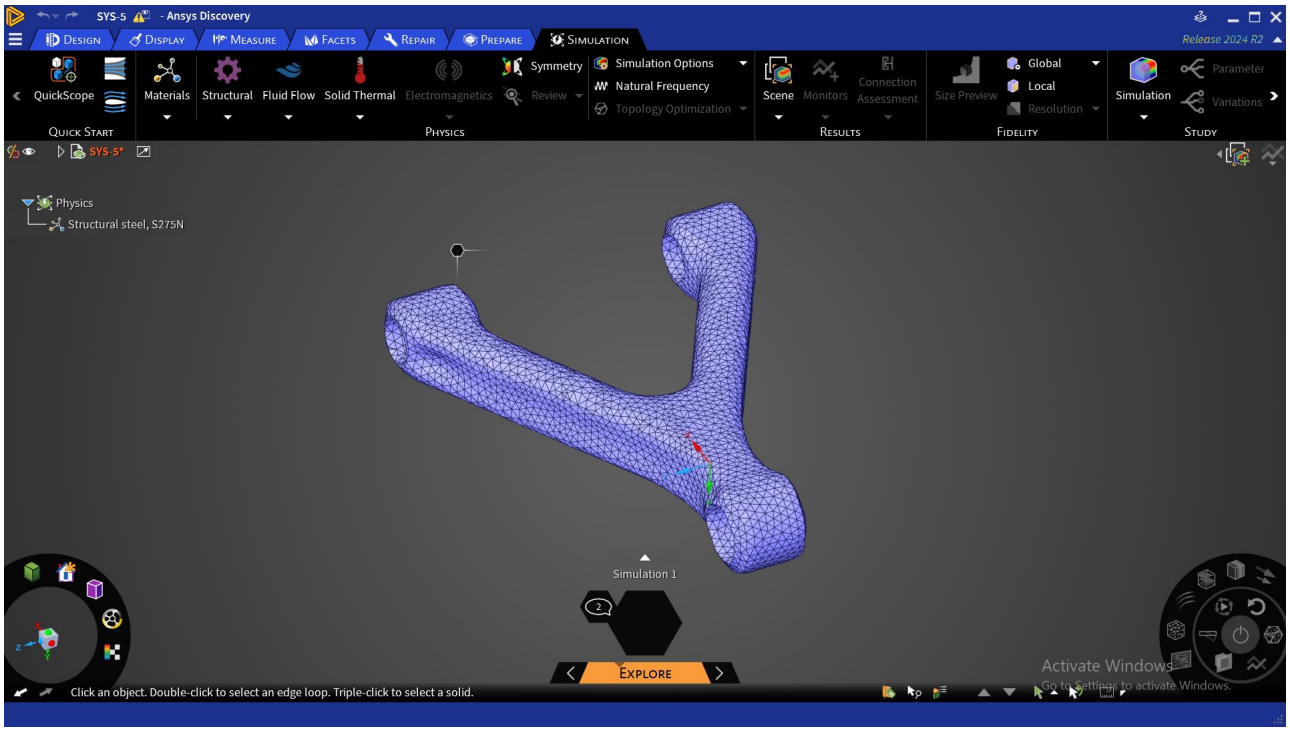

Figure 14: Topology-optimised A-arm geometry in ANSYS Discovery.

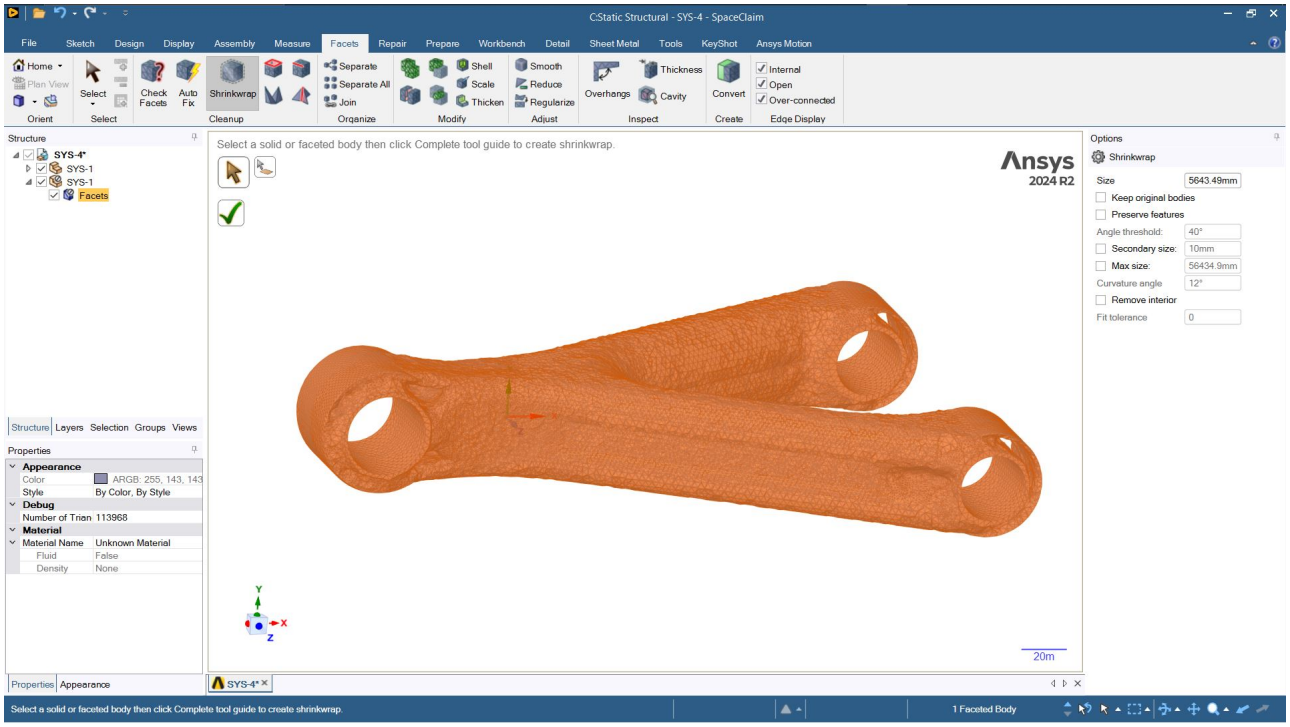

Figure 15: Shrinkwrap – creation of a watertight faceted body around the topology-optimised geometry.

Conversion to solid

The shrinkwrapped facet body is then converted to a solid model using the *Convert to solid* command with face merging enabled (Figure 16). This operation stitches the triangulated surface into larger analytic patches, reduces the number of faces and generates a single solid body that can be meshed robustly in ANSYS Mechanical and used for subsequent validation simulations.

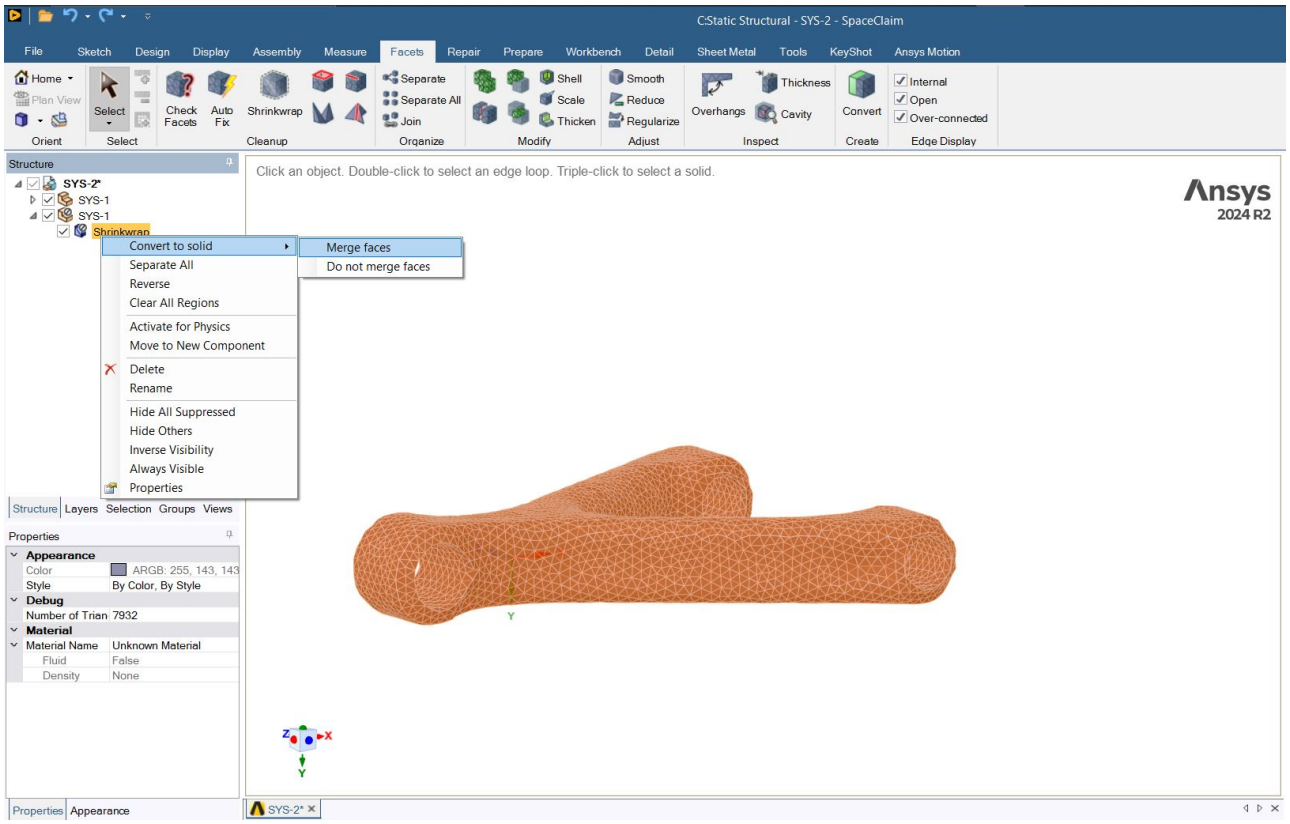

Figure 16: Conversion to solid – merging facets into a single solid body.

Facet error check

Finally, the *Check Facets* tool is used to detect non-manifold vertices, gaps or inverted elements in the repaired mesh (Figure 17). A zero–error report confirms that the cleaned geometry is free of topological defects, ensuring a consistent volume and boundary representation before exporting the solid back to ANSYS Mechanical for structural re-analysis.

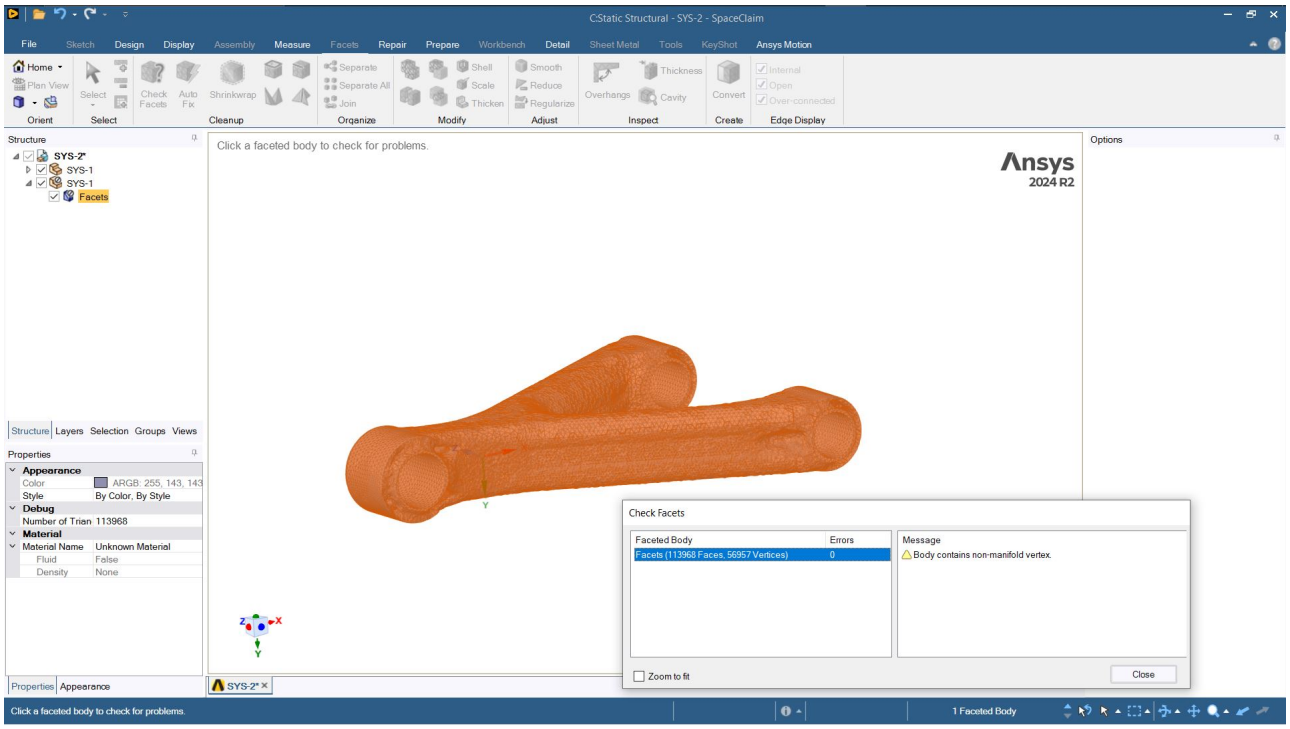

Figure 17: Facet error check – verification of the cleaned faceted body prior to export.

13 Material Selection for Additive Manufacturing

For the topology-optimised A-arm, candidate alloys must support structural performance, fatigue resistance and manufacturability in metal AM:

- Suspension and wheel-end AM demonstrators show that chassis parts demand high stiffness-to-weight ratio and robust fatigue performance under multiaxial loading [2].
- Metal powder-bed fusion processes (e.g., LPBF) are the most mature routes for dense structural AM parts and dictate that materials be available as weldable, fine powders with suitable thermal properties [8].
- Process–structure–property simulations highlight that residual stresses and defects depend strongly on alloy thermal behaviour and scan parameters, so material choice must be consistent with the AM process window [9].
- Automotive AM surveys emphasise cost, qualification status and industrial availability as key criteria in addition to mechanical performance [15].
- Emerging gradient-structured metals offer potential for locally tailored strength and ductility in highly loaded AM components and motivate consideration of future multi-material or graded designs [14].

Table 1: Candidate AM materials for manufacturing the topology-optimised A-arm.

Material family	Example alloy	AM process	Rationale for A-arm application	Reference
Al–Si casting-type aluminium	AlSi10Mg	Laser powder bed fusion (LPBF)	Low density, good specific stiffness and strength after heat treatment; widely used for lightweight automotive AM parts	[4]
Maraging / tool steel	Maraging steel (e.g., 18Ni)	LPBF or DED	High yield strength and good toughness for highly loaded brackets and mounts; demonstrated in direct AM of automotive structural parts	[3]
Stainless / structural steel	Austenitic or martensitic stainless steels	LPBF	Good strength and fatigue resistance with established AM process windows; suitable where corrosion resistance and robustness are prioritised over minimum mass	[8]
Titanium alloy	Ti–6Al–4V	LPBF	Very high specific strength and corrosion resistance, attractive for aggressive lightweighting of suspension links subject to high stress	[4]
Gradient-structured metals	Graded steels / alloys	Advanced LPBF with tailored scan strategies	Conceptual option for future designs where localised gradient microstructures could enhance fatigue resistance in critical fillets while maintaining overall stiffness	[14]

14 Material performance index

For the topology-optimised suspension A-arm, the principal material drivers are specific stiffness, specific strength and suitability for metal additive manufacturing (AM) [2, 3, 4, 8]. Following Ashby's selection methodology, a stiffness-limited index for bending-dominated members may be written as $M_E \propto E^{1/2}/\rho$, while a strength-limited index is $M_\sigma \propto \sigma_y/\rho$, where E is Young's modulus, σ_y is yield strength and ρ is density. Because precise property values are not required at this stage, the candidate alloys from Table 1 are scored qualitatively on a 1–5 scale (5 = best) for:

- S_E: specific stiffness, reflecting $E^{1/2}/\rho$.
- S_σ: specific strength, reflecting σ_y/ρ.
- S_{AM}: AM suitability (process maturity, parameter availability and automotive track record) [8, 3, 15].

A combined, dimensionless material performance index I_j for material j is then defined as

$$I_j = w_E S_{E,j} + w_\sigma S_{\sigma,j} + w_{AM} S_{AM,j}, \tag{8}$$

with weighting factors $w_E = 0.4$, $w_\sigma = 0.3$ and $w_{AM} = 0.3$ to emphasise specific stiffness while still accounting for strength and AM practicality. Table 2 summarises the resulting decision matrix and overall index values (scores 1–5).

Table 2: Decision matrix and material performance index I_j for candidate AM alloys (scores 1–5; higher is better).

Material	S_E	S_σ	S_{AM}	I_j	Rank
AlSi10Mg (Al–Si)	3	3	5	3.6	3
Maraging steel	3	5	4	3.9	2
Stainless / structural steel	3	2	4	3.0	5
Ti–6Al–4V titanium	5	4	4	4.4	1
Gradient-structured metals (concept)	4	4	2	3.4	4

Within the assumptions of this index, Ti–6Al–4V offers the highest combined performance for a lightweight, highly loaded A-arm, followed by maraging steel, while AlSi10Mg provides a good compromise between performance and AM maturity. Gradient-structured metals show promising specific properties but currently score lower on AM readiness because of their limited industrial maturity [14].

15 Decision matrix

Based on the material performance index, the two best candidates for the topology-optimised A-arm are Ti–6Al–4V and maraging steel [2, 3, 4]. Table 3 summarises their scores and final ranking.

Table 3: Reduced decision matrix for the top two candidate materials.

Material	I_j	Rank
Ti–6Al–4V	4.4	1 (preferred)
Maraging steel	3.9	2 (alternative)

Ti–6Al–4V is therefore selected as the primary AM material for the A-arm, with maraging steel retained as a high-strength backup option.

In ANSYS *Engineering Data*, the Ti–6Al–4V alloy is selected from the *Additive Manufacturing Materials* library for the optimised A-arm, as shown in Figure 18.

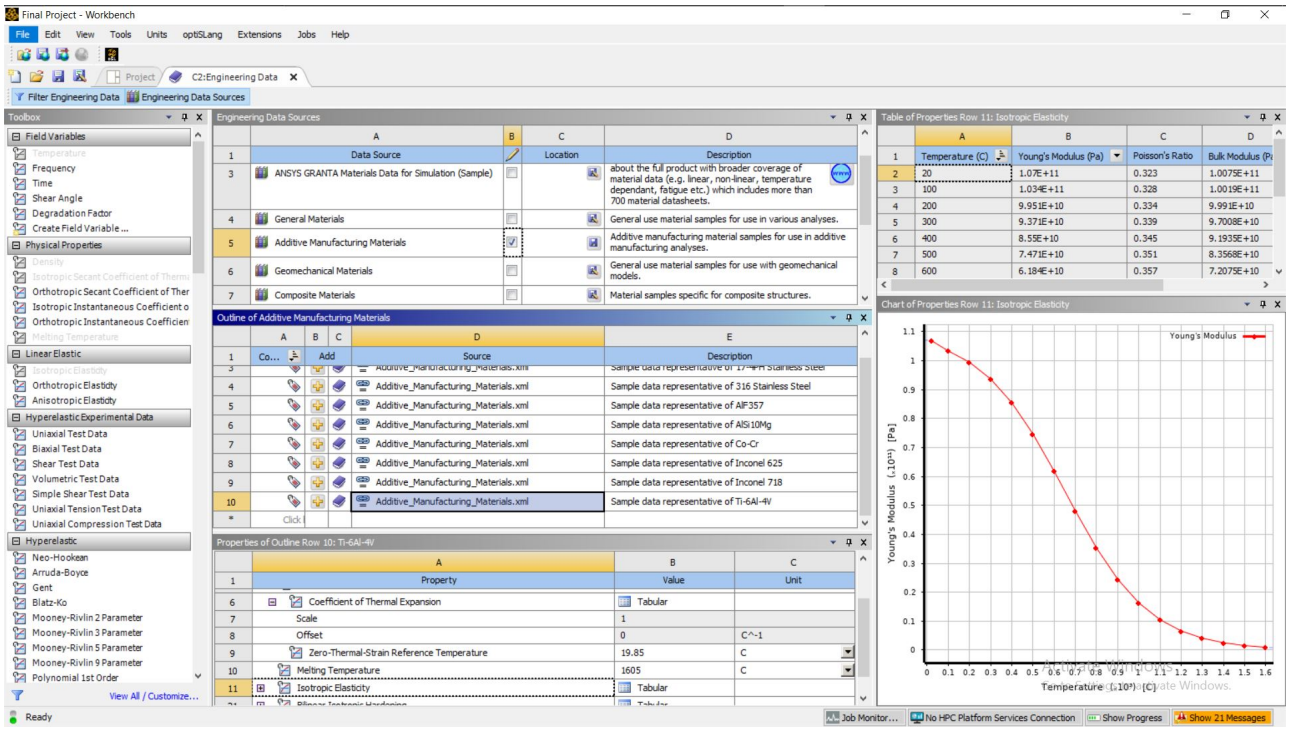

Figure 18: Selection of Ti–6Al–4V from the Additive Manufacturing Materials library in ANSYS Engineering Data.

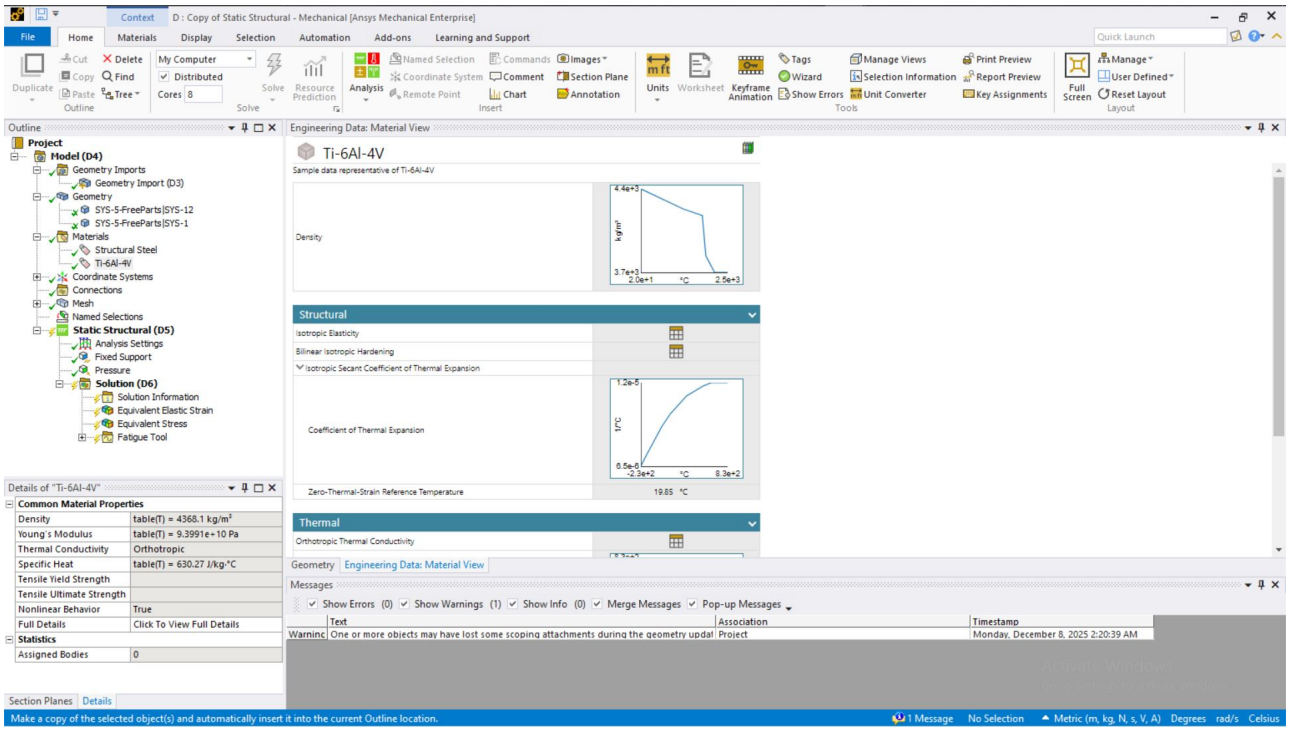

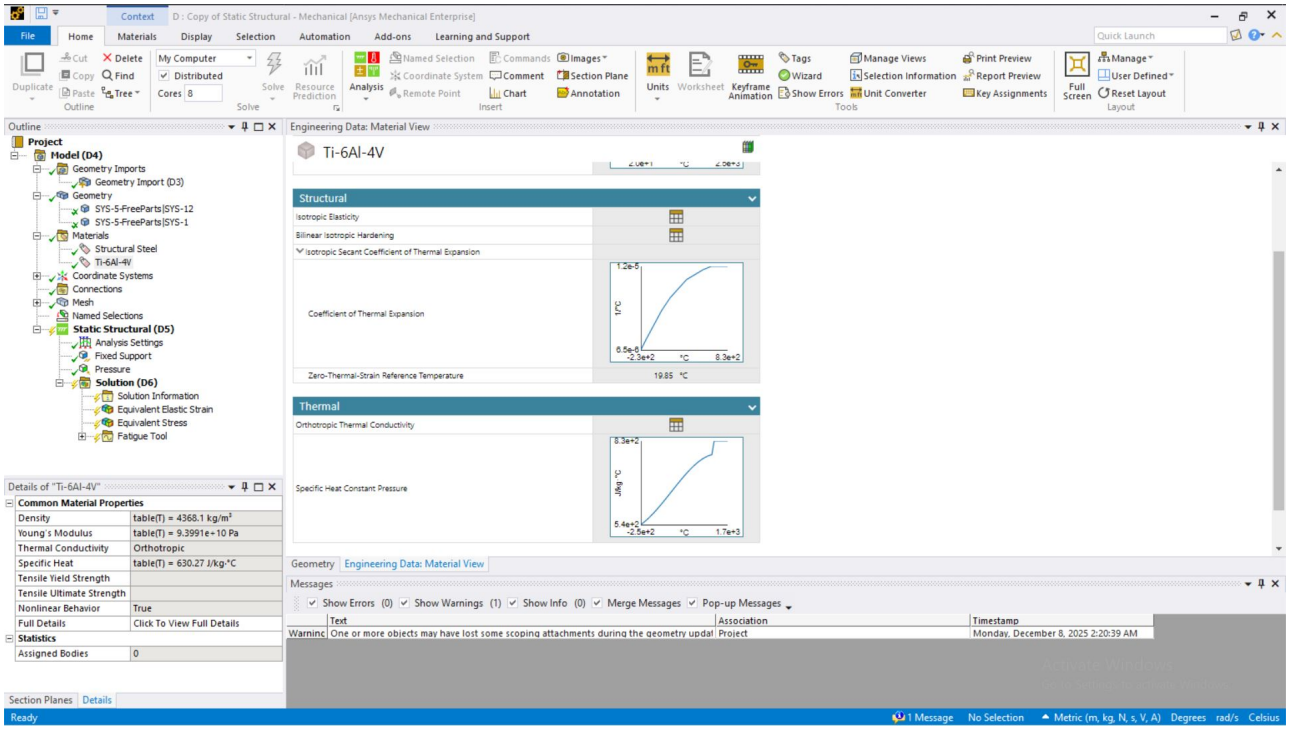

16 Topology-optimised A-arm T.O Geometry Validation: Structural Analysis

After topology optimisation, geometry cleanup and material reassignment, the optimised suspension A-arm is re-analysed under the same static loading and boundary conditions as the baseline steel arm, now using Ti-6Al-4V, the top-ranked material from the performance index and decision matrix. The results below show that the deformation shape and hotspot locations remain consistent with the baseline case, while stresses and strains increase to levels that are still reasonable for Ti-6Al-4V. Overall, the fields look smooth and physically coherent, with no spurious peaks caused by the faceted surface, so the results can be considered qualitatively reliable for static comparison.

TO1 – Equivalent elastic strain distribution

The equivalent elastic strain plot in Figure 19 shows that the maximum strain in the optimised Ti-6Al-4V arm is about 3.9e-3, concentrated at the inner fillet of the loaded bushing. Along the main arms, strain levels drop by an order of magnitude, indicating that stiffness is still governed by the Y-branch region near the joint, similar to the baseline component. Compared with the original steel arm, the strain hotspot is located in the same region but with a higher magnitude, which is consistent with both the reduced mass of the optimised geometry and the lower Young's modulus of Ti-6Al-4V.

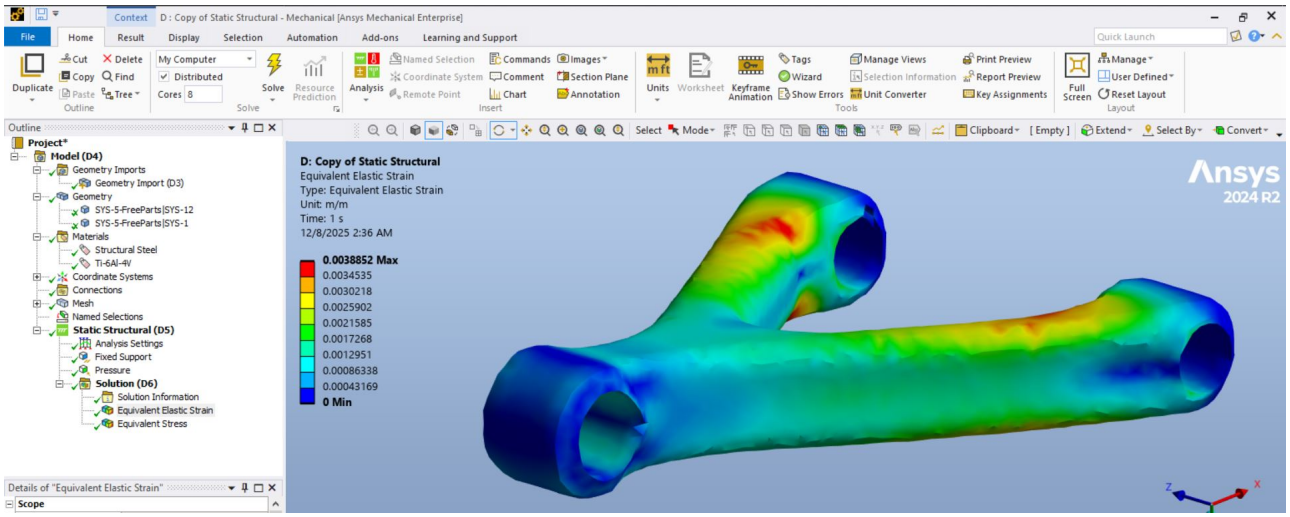

Figure 19: TO1 – Equivalent elastic strain distribution in the topology-optimised Ti-6Al-4V A-arm.

TO1A – Deformed strain field view

Figure 20 provides an alternative view of the same equivalent elastic strain field, highlighting the global bending of the Y-shaped span. The cantilever-like deflection pattern is preserved, and the strain gradient remains smooth from the fixed bushing towards the loaded end. This confirms that the topology optimisation preserved the overall load path while trimming non-critical material from low-strain regions.

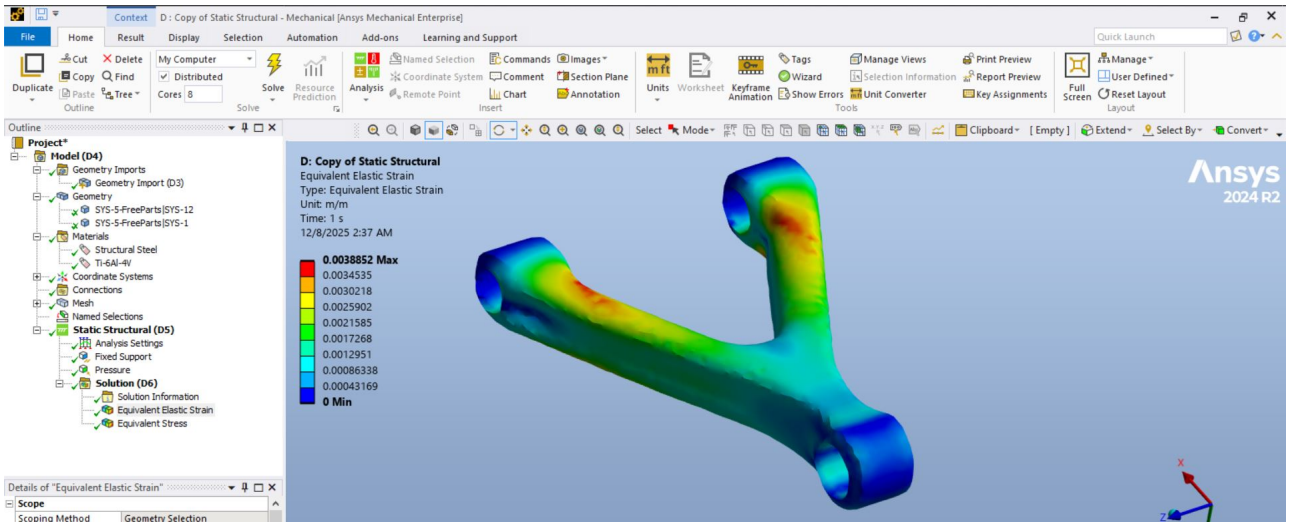

Figure 20: TO1A – Alternative view of equivalent elastic strain in the optimised Ti-6Al-4V A-arm.

TO2 – Equivalent von Mises stress distribution

The equivalent von Mises stress plot in Figure 21 shows a maximum stress of about 4.1e8, again localised at the inner fillet of the loaded bushing. The rest of the arm experiences substantially lower stresses, with large portions of the span working at roughly half of the peak value. This pattern closely matches the baseline steel design, but with higher peak stress due to the reduced cross-sectional area in the optimised geometry. For Ti-6Al-4V, whose static yield strength is significantly higher than that of structural steel, the obtained stress level is still within a realistic static margin, indicating that the mass reduction has not driven the design into an obviously unsafe regime for one load case.

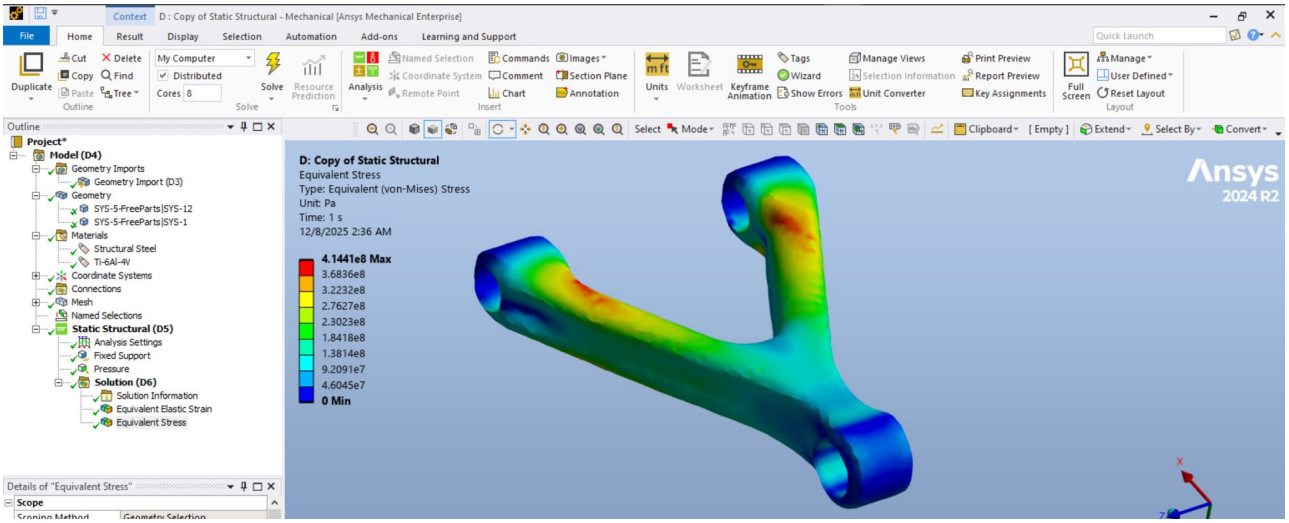

Figure 21: TO2 – Equivalent von Mises stress distribution in the topology-optimised Ti-6Al-4V A-arm.

Comparison between Conventionally fabricated component and Topology optimized component

Table 4: Comparison between the baseline steel A-arm and the topology-optimised Ti-6Al-4V A-arm (approximate values read from FE results).

Metric	**Baseline A-arm (steel)**	**TO A-arm (Ti-6Al-4V)**
Material	Structural Steel	Ti-6Al-4V
Relative mass m/m_0	1.00	0.80
Max von Mises stress $\sigma_{\mathrm{vM,max}}$ [MPa]	≈ 200	≈ 414
Max eq. elastic strain $\varepsilon_{\mathrm{eq,max}}$ [–]	$\sim 1.0 \times 10^{-3}$	$\sim 3.9 \times 10^{-3}$
Approx. yield strength $R_{\mathrm{p0.2}}$ [MPa]	≈ 250	≈ 880
Static safety factor $n_{\mathrm{s}} = R_{\mathrm{p0.2}}/\sigma_{\mathrm{vM,max}}$	≈ 1.25	≈ 2.1
Minimum fatigue life [cycles]	$\sim 2.4 \times 10^{4}$	N/A (no fatigue data)

Discussion and limitations

Comparing these results with the baseline structural steel arm shows that: (1) deformation and strain/stress hotspots remain in the same physical locations (around the loaded bushing fillet and the Y-junction), (2) the overall deflection shape is still consistent with a cantilever arm under end loading, and (3) the increases in strain and stress magnitudes are in line with expectations for a lighter, optimised geometry made from a stiffer-but-lower-density AM alloy. This coherence suggests that the topology-optimised Ti-6Al-4V design is mechanically comparable to the original component under static loading.

However, a full fatigue assessment of the optimised arm cannot be carried out within this model, because the ANSYS material library entry for the selected AM Ti-6Al-4V does not provide the detailed fatigue (S–N) properties required by the fatigue tool. As a result, the present comparison between baseline and optimised designs is limited to static metrics (total deformation, von Mises stress, and equivalent elastic strain).

17 Computational power and limits

All simulations in ANSYS Mechanical, SpaceClaim and Discovery were executed on a personal laptop with the following configuration:

- Operating system: Windows 10 Pro (64-bit).
- CPU: 11th Gen Intel® Core™ i7-1165G7 @ 2.80 GHz.
- RAM: 16 GB.
- GPU: NVIDIA GeForce MX350 (discrete laptop GPU).

This mid-range mobile configuration is adequate for linear static analyses and density-based topology optimisation of a single A-arm, but it imposes practical limits on mesh density and model size. To keep solve times reasonable and avoid running out of memory, the meshes and optimisation settings were chosen as a compromise between accuracy and computational cost, and all results reported in this work were obtained under these hardware constraints.

References

[1] J. Yang, B. Li, J. Liu, Z. Tu, and X. Wu, "Application of additive manufacturing in the automobile industry: A mini review," *Processes*, vol. 12, no. 6, p. 1101, 2024.

[2] F. Weitz, C. S. Debus, M. Frey, and F. Gauterin, "Additively manufactured wheel suspension system with integrated conductions," *Vehicles*, vol. 6, pp. 1051–1069, 2024.

[3] N. Zhao, M. Parthasarathy, S. Patil, D. Coates, K. Myers, H. Zhu, and W. Li, "Direct additive manufacturing of metal parts for automotive applications," *Journal of Manufacturing Systems*, vol. 68, pp. 368–375, 2023.

[4] T. D. Ngo, A. Kashani, G. Imbalzano, K. T. Q. Nguyen, and D. Hui, "Additive manufacturing (3d printing): A review of materials, methods, applications and challenges," *Composites Part B: Engineering*, vol. 143, pp. 172–196, 2018.

[5] K. S. Prakash, T. Nancharaih, and V. V. Subba Rao, "Additive manufacturing techniques in manufacturing – an overview," *Materials Today: Proceedings*, vol. 5, pp. 3873–3882, 2018.

[6] A. Paolini, S. Kollmannsberger, and E. Rank, "Additive manufacturing in construction: A review on processes, applications, and digital planning methods," *Additive Manufacturing*, vol. 30, p. 100894, 2019.

[7] V. Mohanaa, K. S. A. Ali, K. Ranganathan, J. A. Jeffrey, M. M. Ravikumar, and S. Rajkumar, "The roles and applications of additive manufacturing in the aerospace and automobile sector," *Materials Today: Proceedings*, vol. 47, pp. 405–409, 2021.

[8] T. Duda and L. V. Raghavan, "3d metal printing technology," *IFAC-PapersOnLine*, vol. 49, no. 29, pp. 103–110, 2016. IFAC Conference on Manufacturing Modelling, Management and Control.

[9] M. Bayat, W. Dong, J. Thorborg, A. C. To, and J. H. Hattel, "A review of multi-scale and multi-physics simulations of metal additive manufacturing processes with focus on modeling strategies," *Additive Manufacturing*, vol. 47, p. 102278, 2021.

[10] P. Singh, R. M. Singari, and R. S. Mishra, "A review of study on modeling and simulation of additive manufacturing processes," *Materials Today: Proceedings*, vol. 56, pp. 3594–3603, 2022.

[11] H. Shen, L. Pan, and J. Qian, "Research on large-scale additive manufacturing based on multi-robot collaboration technology," *Additive Manufacturing*, vol. 30, p. 100906, 2019.

[12] J. Yang, B. Li, J. Liu, Z. Tu, and X. Wu, "Application of additive manufacturing in automobile industry: A mini review," *Preprints*, 2024. Preprint, not peer-reviewed.

[13] L. Yu, S. Wu, Y. Feng, and C. Zhao, "Development and prospect of additive manufacturing technology in automobile field," *Academic Journal of Science and Technology*, vol. 3, no. 3, pp. 243–246, 2022.

[14] W. Ji, R. Zhou, P. Viveganantham, M. S. Wu, H. Gao, and K. Zhou, "Recent progress in gradient-structured metals and alloys," *Progress in Materials Science*, vol. 140, p. 101194, 2023.

[15] L. Chen, N. P. H. Ng, J. Jung, and S. K. Moon, "Additive manufacturing for automotive industry: Status, challenges and future perspectives," in *2023 IEEE International Conference on Industrial Engineering and Engineering Management (IEEM)*, pp. 1431–1436, IEEE, 2023.